SUPERCONDUCTIVITY

Time-reversal symmetry breaking superconductivity between twisted cuprate superconductors

S. Y. Frank Zhao¹†, Xiaomeng Cui¹†, Pavel A. Volkov^{1,2,3}, Hyobin Yoo⁴, Sangmin Lee⁵, Jules A. Gardener⁶, Austin J. Akey⁶, Rebecca Engelke¹, Yuval Ronen¹, Ruidan Zhong⁷‡, Genda Gu⁷, Stephan Plugge⁸, Tarun Tummuru⁸, Miyoung Kim⁵, Marcel Franz⁸, Jedediah H. Pixley², Nicola Poccia^{1,9}*, Philip Kim¹*

Twisted interfaces between stacked van der Waals (vdW) cuprate crystals present a platform for engineering superconducting order parameters by adjusting stacking angles. Using a cryogenic assembly technique, we construct twisted vdW Josephson junctions (JJs) at atomically sharp interfaces between Bi₂Sr₂CaCu₂O_{8+x} crystals, with quality approaching the limit set by intrinsic JJs. Near 45° twist angle, we observe fractional Shapiro steps and Fraunhofer patterns, consistent with the existence of two degenerate Josephson ground states related by time-reversal symmetry (TRS). By programming the JJ current bias sequence, we controllably break TRS to place the JJ into either of the two ground states, realizing reversible Josephson diodes without external magnetic fields. Our results open a path to engineering topological devices at higher temperatures.

eak van der Waals (vdW) bonding between neighboring atomic layers offers a distinct opportunity for engineering atomic interfaces with controlled twist angles (1). Careful adjustment of the twist angle can create the spatial periodicity of a moiré superlattice (2) with narrow electronic bands and topological structure (3). Such twisted structures of various vdW materials, including graphene (3) and transition metal dichalcogenides (4), have been shown to host a plethora of emergent electronic states, including superconductivity (5), magnetism (6), Chern insulators (7), generalized electronic Wigner crystals (8), and correlated insulating states (9).

Atomically layered cuprate high-temperature superconductors also offer a platform for twistronics by enabling the engineering of the coupling between nodal superconducting order parameters (SOPs) across a twisted vdW interface (*10–15*). In Bi₂Sr₂CaCu₂O_{8+x} (BSCCO), superconducting CuO₂ bilayers are Josephson-coupled through insulating [SrO-

¹Department of Physics, Harvard University, Cambridge, MA 02138, USA, ²Center for Materials Theory, Department of Physics and Astronomy, Rutgers University, Piscataway, NJ 08854, USA. ³Department of Physics, University of Connecticut, Storrs, CT 06269, USA. ⁴Department of Physics, Institute of Emergent Materials, Sogang University, Seoul 04107, Korea. 5Department of Materials Science and Engineering, Seoul National University, Seoul 08826, Korea. Center for Nanoscale Systems, Harvard University, Cambridge, MA 02138, USA. ⁷Department of Condensed Matter Physics and Materials Science, Brookhaven National Laboratory, Upton, NY 11973, USA. 8Department of Physics and Astronomy and Stewart Blusson Quantum Matter Institute, University of British Columbia, Vancouver, BC V6T 1Z4, Canada. ⁹Leibniz Institute for Solid State and Materials Research Dresden (IFW Dresden), 01069 Dresden, Germany, *Corresponding author. Email: n.poccia@ifw-dresden.de (N.P.); pkim@physics.harvard.edu (P.K.)

†These authors contributed equally to this work. ‡Present address: Tsung-Dao Lee Institute and School of Physics and Astronomy, Shanghai Jiao Tong University, Shanghai 200240, China. BiO] bilayers (16), where the crystal can be mechanically cleaved into atomically flat crystals (17, 18) exhibiting high-temperature superconductivity even in the monolayer limit (19).

Josephson junctions (JJs) formed at twist boundaries between cuprate crystals directly probe the pairing symmetry of Cooper pairs (20, 21). For example, using ab-planar tilt grain boundaries, measurements of angle-dependent critical currents (22), nonsinusoidal Josephson current-phase relations (23), and spontaneous supercurrents (21) established the cuprates as d-wave superconductors where the SOP changes sign when Cooper pair momentum is rotated by 90°.

Similarly, interfacial Josephson coupling between twisted nodal d-wave superconductors is strongly modulated by the twist angle (15). Particularly, at a twist angle of $\theta = 45^{\circ}$, direct Cooper pair tunneling is forbidden because of the complete mismatch between the $d_{x^2-y^2}$ symmetric SOPs across the interface (15). Any remaining Josephson supercurrents are mediated through second-order processes (10-12, 24); the system is expected to support topological time-reversal symmetry (TRS)-breaking superconducting phases persisting up to the junction superconducting transition temperature $T_{\rm C}$ (11, 12). Alternatively, TRS can be broken away from $\theta = 45^{\circ}$ by an applied current, which is predicted to induce a topological superconducting state (13).

Building twisted BSCCO junctions

The preservation of surface superconductivity of BSCCO crystals after vdW stacking remains an outstanding experimental challenge (17, 18). BSCCO crystals react with moisture (19, 25), and their oxygen dopants become mobile above 200 K (19, 26). BSCCO twist junctions previously required high-temperature oxygen annealing to restore interfacial superconductivity

(27-3I), often at the cost of considerable in facial structural reconstruction (29, 3I-33), pressed $T_{\rm C}$ (28-3I), low critical current density $J_{\rm C}$ at zero twist angle (27-29, 3I), and pronounced anomalies in the resistance-temperature (R-T) curves (28, 29, 3I). Most experiments observed no angular sensitivity (27-29), except two (30, 3I) where the Josephson coupling angular dependence deviated strongly from conventional models of d-wave superconductivity (15).

We overcome these challenges by developing a cryogenic, solvent-free vdW transfer technique in pure argon using a liquid nitrogencooled stage kept at <-90°C. We cleave an exfoliated BSCCO crystal into two copies between BiO planes, while thermally freezing out oxygen migration and other chemical processes at the surface (Fig. 1A and fig. S1). One of the crystals is quickly rotated to the targeted twist angle and reassembled with the other. A Josephson junction forms in the overlapping region upon contact (Fig. 1, B to D). Two sets of electrical contacts, both defined by stencil masks and evaporated on a -30°C cold stage (17), are prefabricated nearby before cleaving and placed on the top surface of the bottom crystal after reassembly. This contact geometry probes the twist junction while minimizing bulk crystal contributions (Fig. 1H, upper inset). Additional details are given in section S1 of (34).

Cryogenic handling in argon is critical to maintaining pristine atomic interfaces without interfacial reconstruction and oxygen dopant changes. Figure 1D shows cross-sectional highangle annular dark field (HAADF) scanning transmission electron microscope (STEM) image of a $\theta = 46^{\circ}$ junction, simultaneously viewing both BSCCO crystals on two different zone axes. Notably, crystalline order is maintained at the interfacial layer with no change to the lattice structure (35) in the [001] direction between atomic layers (Fig. 1E) or along CuO₂ planes (Fig. 1, F and G, and figs. S2 to S4). Detailed analysis of the interfacial BiO atomic layer places an upper bound of the twist-angle disorder below 0.2° [section S2 of (34)]. Similar interface quality is uniformly observed across large areas in several additional junctions (see figs. S2 to S4, for example). We compare 26 devices with θ ranging from 0° to 180°, with $T_C >$ 79 K and average $T_{\rm C}$ of 84 K (Fig. 1H, lower inset), demonstrating high oxygen dopant uniformity even at the junction. Neither T_C nor the normal-state conductivity are systematically correlated with θ (fig. S8).

At $\theta=0^\circ$, our devices exhibit electronic characteristics similar to the intrinsic Josephson junctions (IJJs) that naturally form between CuO₂ layers in BSCCO single crystals (16), demonstrating the high interfacial quality of our JJs. Figure II shows the current-voltage (I-V) characteristics (IVCs) measured with four terminals at temperature T=9 K. In this low-temperature regime, the JJ exhibits a large hysteresis. As we

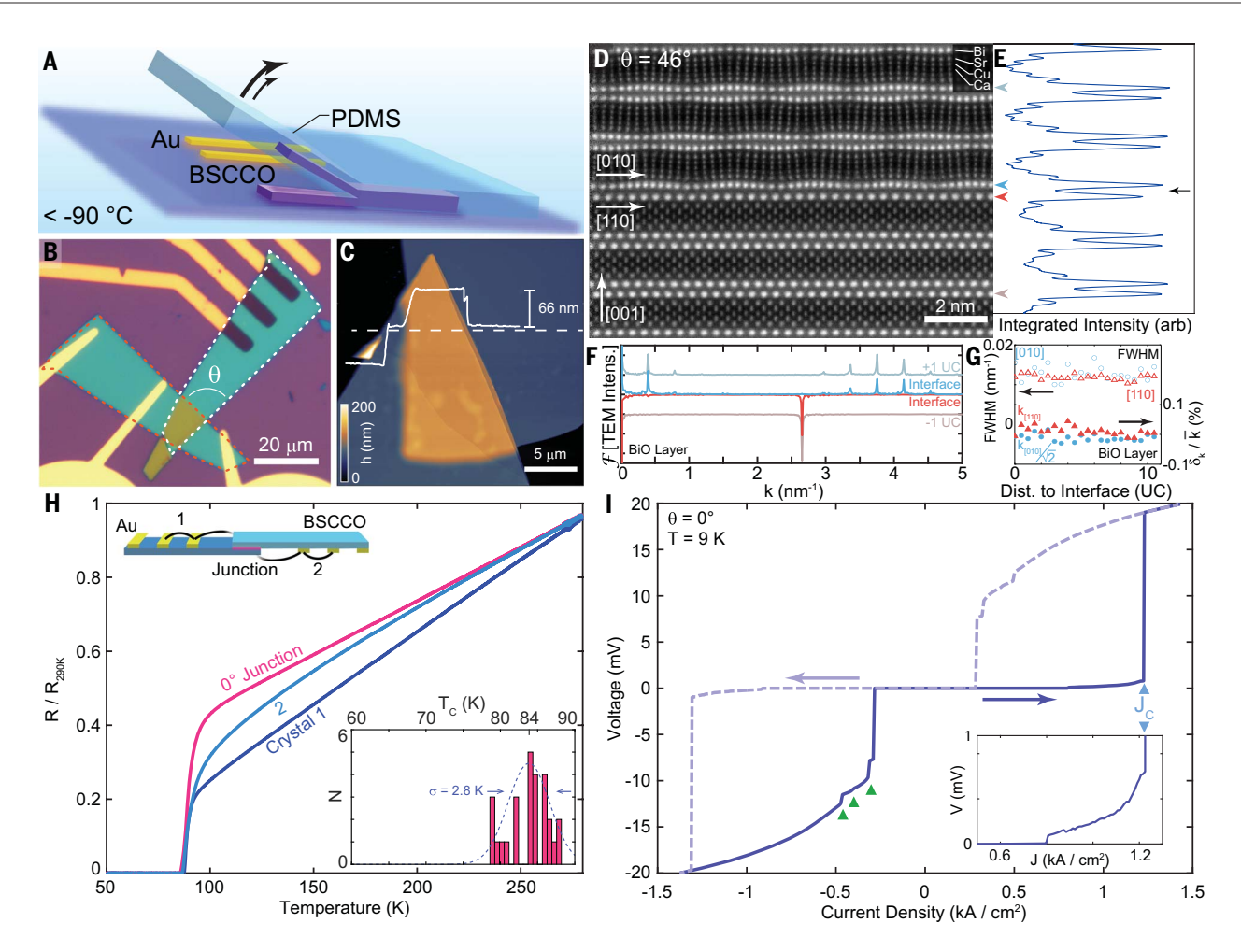


Fig. 1. Twist Josephson junctions with intrinsic junction quality.

(A) Schematic of key fabrication step: a single BSCCO crystal is cleaved using polydimethylsiloxane (PDMS) below -90° C. (B) Optical micrograph of a BSCCO twist junction. Dashes outline identical copies of the same crystal. Corresponding schematic in upper inset of (H). (C) Atomic force microscope topography showing atomically flat interface. Line trace shows topography along dotted line. (D) Cross-sectional annular dark field scanning TEM image of θ = 46° junction, showing bulk-like crystalline order at the interface. Bright spots are columns of atoms identified in the upper right corner. (E) Integrated intensity of each layer. arb, arbitrary units. (F) Fourier transform of TEM line cuts at BiO layers

highlighted in (E), showing atomically sharp structural transition at the interface. (**G**) BiO layer lattice periodicity variation, δ_k/\bar{k} , and peak full width at half maximum (FWHM) from (F), whose fluctuations are within 0.05%, with peak FWHM at fast Fourier transform resolution (0.014 nm $^{-1}$). (**H**) In-plane resistance in each bulk crystal versus resistance through the artificial junction between them, showing nearly identical junction $T_{\rm C}$. Lower inset shows $T_{\rm C}$ distribution among all 26 JJs in the angle-dependence analysis. (**I**) *I-V* curve for a $\theta=0^{\circ}$ junction in both sweep directions (arrows). Blue triangle highlights $J_{\rm C}$ comparable to IJJs. Green triangles highlight inelastic scattering features seen at the same voltages in IJJs (*16*). Inset shows low-voltage region of IVC.

increase current bias from a large negative value, the resistive quasiparticle branch of the IVC undergoes a series of jumps (green arrows) before retrapping into the superconducting state. Similar jumps were seen in IJJs [see section S5 of (34)] (16). Under positive bias current, V first becomes nonzero at I_{C1} (Fig. 1I, inset) before jumping about 20 mV to the resistive state at the critical current $I_{\rm C}$, marked by the blue triangle. The small voltage rise at I_{C1} was previously seen in some IJJs (16, 36, 37) and was attributed to self-field effects (16, 38), whereas the V jump at I_C is comparable in magnitude to the corresponding jump in IJJs (16, 39, 40). Upon reversing the bias current polarity (dashed line), the JJ's I-V behavior is mirrored along I=0. Normalizing to junction area, we obtain a critical current density $J_{\rm C}\approx 1.2~{\rm kA/cm^2}$ for this junction, similar to the $J_{\rm C}$ of intrinsic junctions (41). Together, these observations indicate that our $\theta=0^{\rm o}$ JJ reaches electronic quality comparable to IJJs of single-crystal BSCCO.

Twist angle and temperature-dependent transport

To compare transport characteristics of different twisted JJs, we normalized the bias current I with the junction normal resistance $R_{\rm N}$ [see section S4 of (34) for experimental definition]. Because $I_{\rm C}$ and $R_{\rm N}^{-1}$ are both proportional to the area of the junction, the product $I_{\rm C}R_{\rm N}$ is independent of junction area. Figure

2A shows the normalized dynamic resistance $[dV/dI]/R_{\rm N}$ as a function of T and $IR_{\rm N}$ at $\theta=0^\circ$, 31°, and 44.9° (similar data for 26 JJs studied are shown in fig. S11). Several features are apparent in these datasets. First, as the current sweeps from left to right, on the retrapping side $(IR_{\rm N}<0)$, constant-voltage inelastic tunneling features appear in arcs of constant V. Next, on the switching side $(IR_{\rm N}>0)$, both V and dV/dI jump at critical current $I_{\rm C}$, which depends on T. The detailed behavior of $I_{\rm C}(T)R_{\rm N}$ depends on θ , as we detail below. Finally, we find the hysteresis of JJs to be reduced in the high-temperature regime as $I_{\rm C}(T)R_{\rm N}$ decreases.

The analysis of $I_{\rm C}R_{\rm N}$ for 26 devices with θ between 0° and 180° indicates that the magnitude

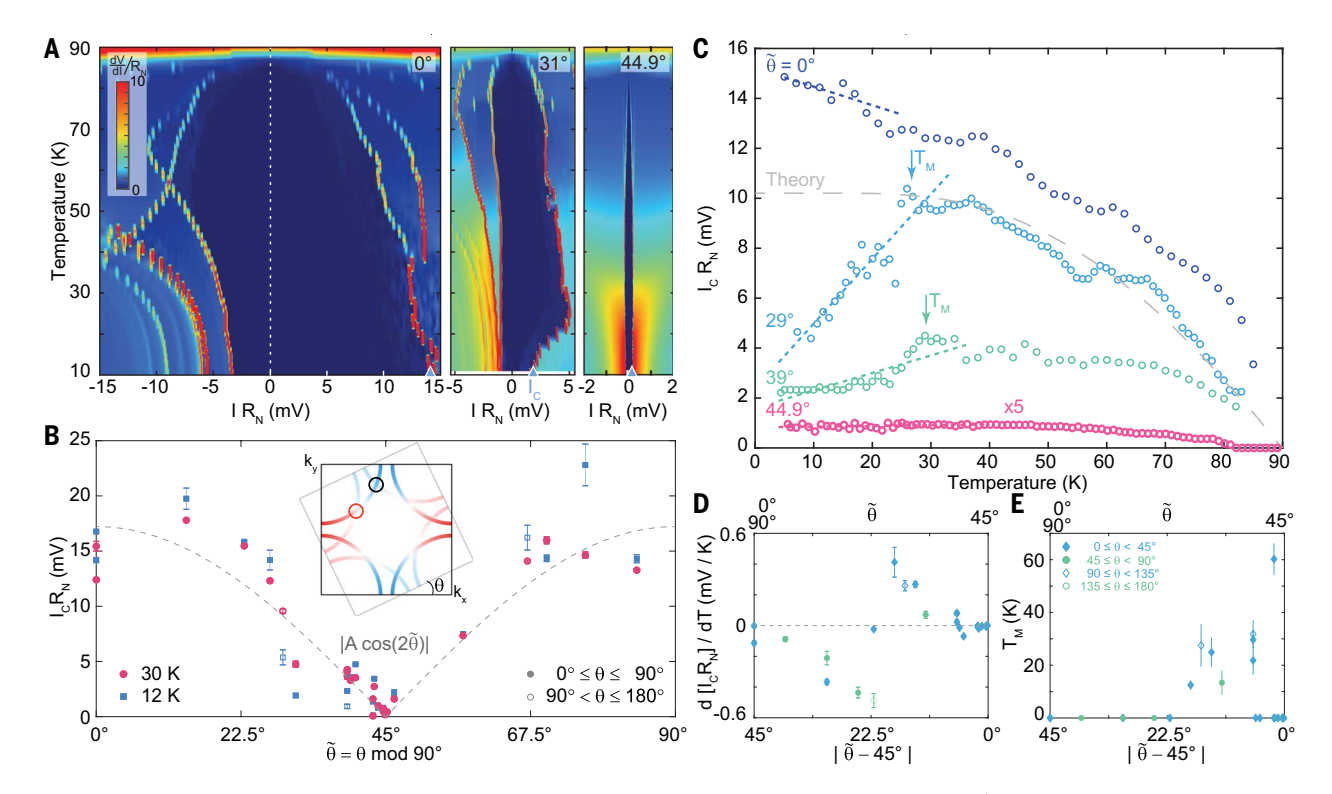


Fig. 2. d-wave SOP symmetry revealed by supercurrent tunneling.(A) Normalized differential resistance $[dV/dI]/R_N$ versus characteristic voltage IR_N and temperature T. Current is swept to the right. Blue arrows highlight I_CR_N .

(B) Angular dependence of I_CR_N at 30 and 12 K. The points follow the $|\cos(2\bar{\theta})|$ curve predicted for nearly incoherent tunneling between d-wave superconductors (15). (Inset) Schematic diagram of the Fermi surface of both crystals, with sign and

magnitude of superconducting gap $\Delta(\vec{k})$ superposed in color. At $\theta > 10^\circ$, Fermi surfaces intersect at two points per quadrant (circles) with different relative signs of SOPs. (**C**) Temperature dependence of the critical current for select devices. Dashed lines are linear fits to the low-temperature data. $T_{\rm M}$ is the temperature where $I_{\rm C}$ is maximal. Gray theory line shows expected $I_{\rm C}R_{\rm N}(T)$ behavior [see section S8 of (34)]. (**D**) The slope of the low-temperature linear fit, $d(I_{\rm C}R_{\rm N})/dT$. (**E**) $T_{\rm M}$ as a function of angle $\tilde{\theta}$.

of I_CR_N becomes smaller closer to 45° and 135°, where the JJs also appear less hysteretic. In Fig. 2B, we plot I_CR_N at two representative temperatures, 12 and 30 K, as a function of a new variable $\tilde{\theta}=\theta$ mod $\pi/2$. We observe that I_CR_N ($\tilde{\theta}$) follows $\left|\cos\left(2\tilde{\theta}\right)\right|$, which is expected for nearly incoherent Cooper pair tunneling between d-wave superconductors (15). Similar angular dependence is seen in junction critical current density and junction voltage just above the critical current $V(I_C)$ (see fig. S8). In conventional tunneling JJs, $eV(I_C)\approx 2\Delta$ (42). In BSCCO IJJs, $eV(I_C)$ usually reaches about half the spectroscopic gap value (16).

The temperature dependence of Josephson coupling in our twisted junctions provides further insight into the pairing symmetry of the Cooper pairs in BSCCO. Figure 2C shows $I_{\rm C}(T)R_{\rm N}$ for several representative JJs with different $\tilde{0}$. For $\tilde{0} \sim 0$, we find that $I_{\rm C}(T)R_{\rm N}$ monotonically decreases as T increases, approximately following the theory curve for nearly incoherent tunneling between d-wave superconductors [dashed line; see section S8 of (34)]. As $\tilde{0}$ increases, however, a surprising nonmonotonic behavior of $I_{\rm C}(T)R_{\rm N}$ appears. For example, for $\tilde{0} = 29^{\circ}$ and 39° in Fig. 2C, $I_{\rm C}(T)R_{\rm N}$ increases alongside T, reaching a maximum value at $T = T_{\rm M}$, and then decreases as T approaches $T_{\rm C}$.

More quantitative analysis can be found in Fig. 2, D and E, where we plot the low-temperature slope $d(I_CR_N)/dT$ (dashed lines in Fig. 2C and fig. S12) and observed $T_{\rm M}$, respectively. These plots show a nonmonotonic behavior of $I_CR_N(T)$, signaled by the positive slope of $I_CR_N(T)$ at low temperatures with finite $T_{\rm M}$, appearing within $\left|\tilde{\theta}-\pi/4\right|<\pi/8$.

The strong $\tilde{\theta}$ dependence of the nonmonotonic $I_{\rm C}(T)R_{\rm N}$ in Fig. 2, D and E, points to SOP d-wave symmetry as its origin. For this explanation, we consider a gap function $\Delta_{1,2}(\mathbf{k})$ superimposed on top of the Fermi surface $E_{\rm F}^{1,2}(\mathbf{k})$ (43), where **k** is the in-plane Cooper pair wave vector in the first Brillouin zone and the index 1 or 2 denotes the top and bottom layer of BSCCO, respectively. In the twisted JJ, $E_{\rm F}^1(\mathbf{k})$ and $E_{\rm F}^2(\mathbf{k})$ are rotated relative to each other by angle θ (Fig. 2B, inset). At $\theta \approx 0$, $E_{\rm E}^1(\mathbf{k})$ and $E_{\rm F}^2(\mathbf{k})$ overlap almost completely and $\Delta_1(\mathbf{k})\Delta_2(\mathbf{k})$ is >0, yielding a uniformly positive contribution to critical current for coherent tunneling (15). As θ increases to ~10°, the Fermi surfaces overlap at two points per quadrant in k-space, but with opposite phase difference between layers, yielding nodal and antinodal contribution where $\Delta_1(\mathbf{k})\Delta_2(\mathbf{k})$ alternates in sign. Because the supercurrents from these two components carry the opposite sign, their contributions to the total critical current compete. As the gap in the nodal region is much smaller than the antinodal one, nonmonotonic temperature-dependent $I_{\rm C}(T)$ is expected for $\tilde{\theta} \approx \pi/8$, where the competition is strongest [see section S8 of (34) and (44) for more quantitative discussion]. We also note that near $\tilde{\theta} \approx \pi/4$, the JJ coupling is strongly suppressed but remains nonzero. For the $\theta = (44.9 \pm .1)^{\circ}$ junction, Josephson critical current can be measured up to 79 K, with $I_{\rm C}R_{\rm N}$ about two orders of magnitude smaller than the 0° value.

Second-order Josephson coupling near θ = 45°

The origin of the finite supercurrent near 45° is encoded in the Josephson current-phase relation (CPR) $j(\phi) = j_1 \sin(\phi) + j_2 \sin(2\phi)$, where j and ϕ are the Josephson current density and phase, respectively (10, 12, 24). At $\tilde{\theta} = 45^{\circ}$, the maximally mismatched SOP phase eliminates the conventional direct Cooper pair tunneling term j_1 . The supercurrent must then flow through second-order mechanisms, which are predicted to support an interfacial superconductivity with doubly degenerate Josephson energy owing to the inherent $d_{x^2-y^2}$ symmetry of the SOP within each flake (10–12). The CPR corresponding to this unusual SOP leaves an experimental signature in the in-plane magnetic

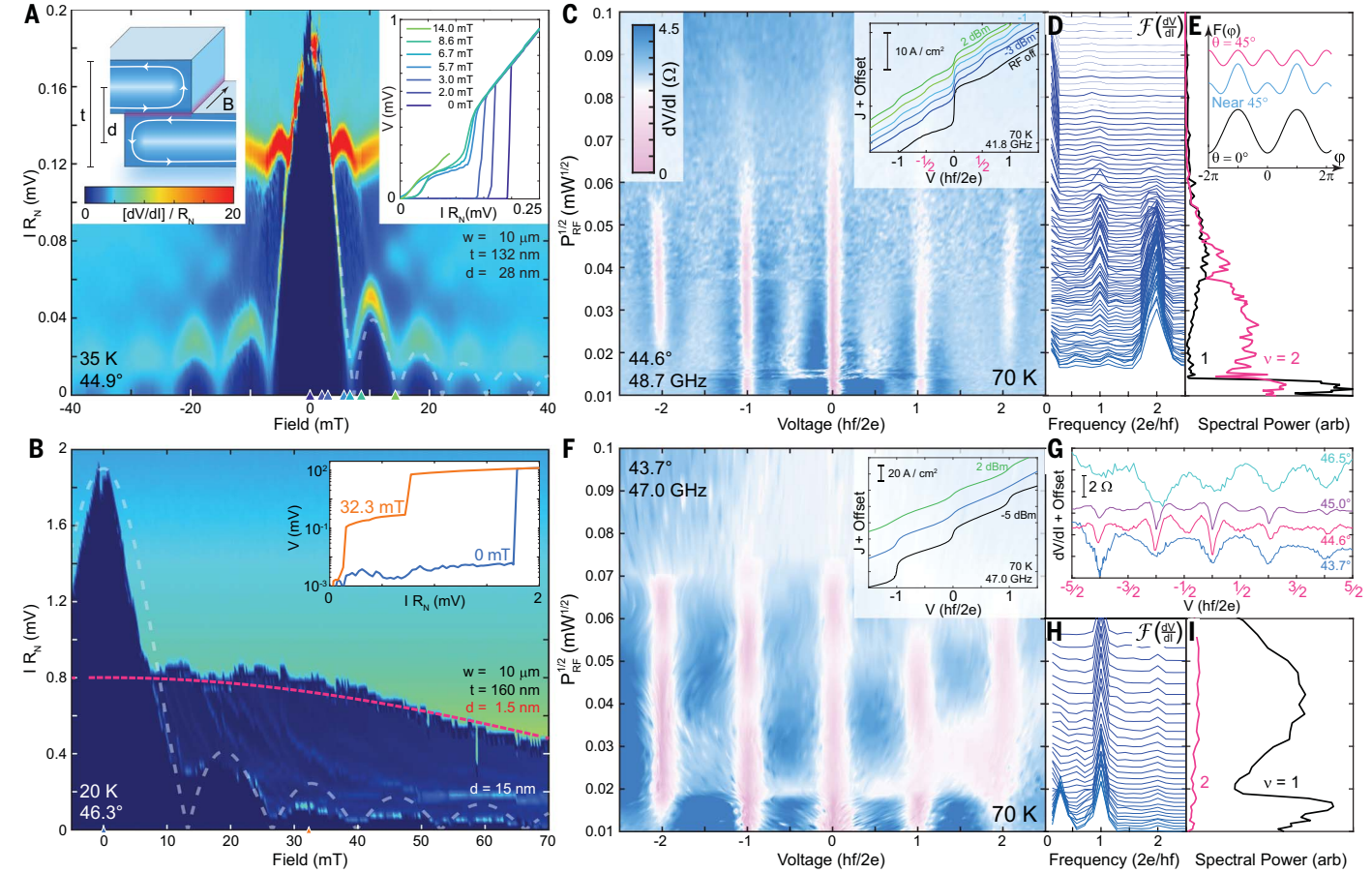


Fig. 3. Half-integer Shapiro steps and magnetic interference patterns emerge close to θ **= 45°. (A)** Response to in-plane magnetic field $B_{||}$ at θ = 44.9°. One well-developed Fraunhofer pattern corresponding to d = 28 nm (14 nm for a second-harmonic CPR) appears, as indicated by the gray dashed line. (Left inset) Junction schematic. The Meissner currents (white lines) in the flakes affect the phase difference at the twist junction, enhancing its effective thickness d for the magnetic flux (42) [see section S13 of (34)]. (Right inset) IVCs at fields highlighted with arrows in the main panel. **(B)** θ = 46.3° JJ. Two Fraunhofer patterns with different magnetic field periodicity appear (dashed lines), with an estimated d = 15 nm (gray) and d =1.5 nm (red). (Inset) *I-V* characteristics at two different

 $B_{||}$ values, showing two jumps in V. (C) $\theta=44.6^{\circ}$ JJ. dV/dl as a function of voltage across the junction and microwave illumination power $P_{\rm RF}^{1/2}$ at 70 K. dV/dl dips (white, pink) correspond to Shapiro steps. (Inset) I-V characteristic with half-integer Shapiro steps. (D) Fourier transform of dV/dl(V) and (E) the spectral power at $v_f=1$ and 2·2e/hf for the $\theta=44.6^{\circ}$ JJ. (Inset) Schematic of the junction free energy F versus Josephson phase ϕ as twist angle changes. At 45°, the second harmonic dominates the current-phase relation. (F, H, and I) As in (C) to (E), but for the 43.7° device, where only integer Shapiro steps appear. (G) Representative dV/dl for all four devices with Shapiro step measurements at different twist angles. Half-integer Shapiro steps are only observed in junctions closest to 45°.

interference ("Fraunhofer") pattern and microwaveinduced Shapiro steps in the IVC, which are both sensitive to the presence of two degenerate local minima in Josephson energy that are connected by TRS (10, 11, 24).

Figure 3, A and B, shows Fraunhofer interference patterns (FIPs) obtained at two different angles by applying parallel magnetic field B_{\parallel} . Figure 3A shows $\theta=44.9^{\circ}$ JJ with $I_{\rm C}(B_{\parallel})$ oscillation with a period about 20 times shorter than that expected for intrinsic junctions. At a nearby angle $\theta=46.3^{\circ}$ (Fig. 3B), the short-period oscillations appear to coexist with a long-period oscillation characteristic of IJJs (41). A reduction in the FIP period implies an increase in d, the thickness of the interfacial region where magnetic field penetrates owing to field-induced currents extending into the

crystal bulk (42). The ratio d/t, where t is the total junction thickness, depends only on the properties of the crystal and junction geometry and should not depend strongly on the twist angle [see section S13 of (34)]. Notably, for the devices in Fig. 3, A and B, which share similar geometry, we obtain $d/t \approx 0.1$ for both devices only if we assume that the 44.9° junction is coupled purely through the second-order process with a doubled FIP period.

The presence of higher-order harmonics in the CPR near 45° is further revealed by measuring Shapiro steps in I-V under microwave illumination of frequency f (Fig. 3, C and F, inset) (II, 24). In conventional JJs, where the CPR is dominated by the first harmonic of φ , Shapiro steps appear as plateaus of constant voltage whenever V approaches $n \cdot hf/2e$, where

n is an integer. We observe these conventional integer Shapiro steps in the JJs substantially away from $\hat{\theta}=\pi/4$, as shown in the $\theta=43.7^{\circ}$ device (Fig. 3F). Consistent with the FIP discussed above, the experimentally observed Shapiro steps also show signatures of the second-harmonic CPR as $\hat{\theta}$ approaches $\pi/4$ (Fig. 3C): specifically, when our devices are within $(45\pm1)^{\circ}$, additional steps at half-integer n appear. As shown in Fig. 3C, microwave illumination causes a series of dV/dI dips corresponding to steps in I-V at both integer and half-integer n to emerge from the symmetric I-V curve of an overdamped JJ.

The Fourier components of dV/dI(V) show the relative strengths of integer and half-integer Shapiro steps. For the conventional Shapiro steps appearing in the 43.7° device, the Fourier

transform shows dominant spectral power for the first harmonic $v_1 = 2e/hf$ (Fig. 3, H and I). In contrast, for the devices exhibiting half-integer Shapiro steps (e.g., the 44.6° device at low microwave power), the Fourier transform is dominated by the second harmonic $v_2 = 4e/hf$. The corresponding dV/dI shows dips of similar strength at half-integer and integer steps, indicating that second-order processes dominate over the conventional Josephson coupling close to 45° .

Similar second-harmonic Josephson effects have been observed in parallel-connected arrays of 0- and π -JJs, where multiple degenerate ground states can form (45–48). Electronically, Josephson currents across distributions of facets in such junctions create disordered magnetic interference patterns, often with prominent peaks symmetrically centered about zero magnetic field (49–52). This is at odds with our Fraunhofer-like $J_{\rm C}(B_{\parallel})$ measurements. Moreover, our TEM analysis [see section S2 of (34)] quantitatively bounds our interfacial twist angle disorder to 0.2°, which excludes the scenario

of angle inhomogeneity-induced TRS breaking in this device (53).

Current-trainable Josephson diode effect

The sign of j_2 in CPR plays an important role in the quantum properties of twist Josephson junctions when it exceeds j_1 in magnitude. When j_2 is negative, the JJ ground state splits into a pair of degenerate states with complex phase angle $\varphi = \pm \varphi_0$ lying between 0 and π (12, 24) (Fig. 3E, inset). When θ is tuned slightly away from 45°, both CPR harmonics coexist, creating asymmetric potential barrier heights around each of the degenerate energetic minima. We observe such TRS breaking through an asymmetric critical current, when the Josephson phase particle begins to roll down the resistively and capacitively shunted Josephson (RCSJ) washboard potential at different tilt angles, corresponding to different bias currents, in each direction (Fig. 4A, schematic) (54).

We find that twist JJs slightly away from $\theta=45^{\circ}$ exhibit nonreciprocal Josephson critical current, which can be controlled by the

current sweep sequence. In this scheme, one can controllably prepare the TRS broken initial $\pm \phi_0$ states by the "training current sequence," as shown in Fig. 4A. We use both positive and negative direction (+/-) and full and half sweep (F/H) to control the location of the phase particle during the retrapping process with high probability (24), where the switching critical current density $J_{\rm C\pm}^{\rm F/H}$ is defined from supercurrent to normal current transition. We note that $J_{\rm C+}^{\rm F/H} \approx -J_{\rm C-}^{\rm F/H}$, reflecting the symmetry between $\pm \phi_0$ states due to TRS in the absence of magnetic field.

Controlled placement of Josephson phase particles in a specific $\pm \phi_0$ valley (broken TRS) and the directionally asymmetric barrier associated with each valley (broken spatial inversion symmetry) are the critical ingredients for a Josephson diode (55–64), as shown in Fig. 4, B and C. Here, by biasing the "training" current into the voltage state in the forward (reverse) direction with the amplitude between $\left|J_{C\pm}^{F/H}\right|$, and then back to zero, the running JJ phase particle is retrapped into the $-\phi_0$ (or $+\phi_0$) valleys,

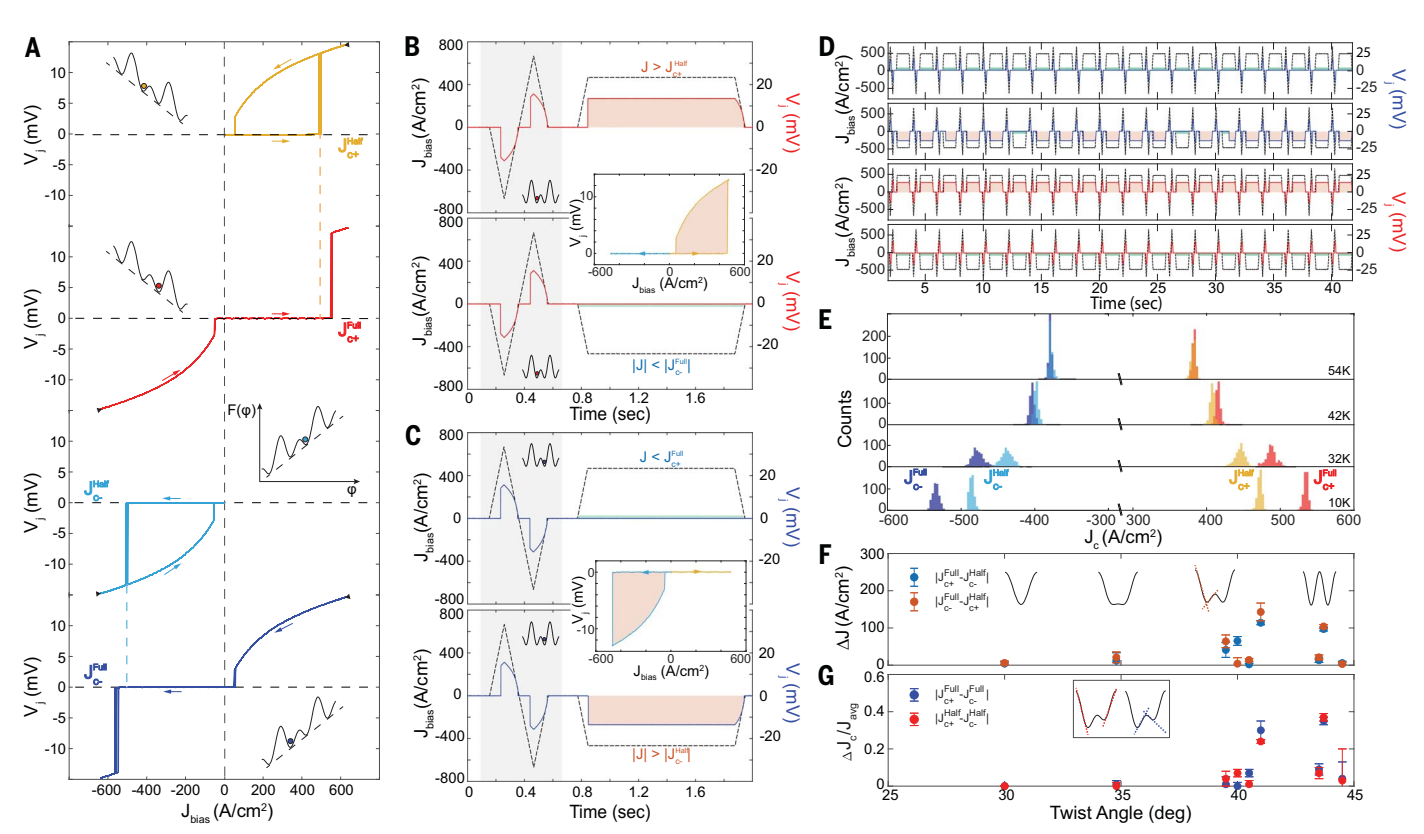


Fig. 4. Time-reversal symmetry breaking Josephson diode effects. (A) Junction *I-V* characteristics obtained from a JJ with θ = 39.5° at 12 K, revealing four distinct $J_{\rm C}$ accessible via different current sweep directions and histories. Schematics show RCSJ phase particle on the washboard potential just before reaching $J_{\rm C}$. (B and C) Junction current bias (dashes) and voltage response (lines) across training (gray shading) and test pulses. For each subpanel, identical training pulses place the RCSJ phase particle in the same state (schematics). Insets show IVC of each test pulse. (D) Junction response to consecutive training and test pulses, showing controllable behavior.

(**E**) Temperature-dependent switching current distributions of the four different critical currents. (**F**) Difference between mean full and half sweep $\Delta J = \left|J_{\text{C}\pm}^{\text{F}/\text{H}} - J_{\text{C}\pm}^{\text{H}/\text{F}}\right|$ versus twist angle θ , and the standard deviation measured at 30 K. Schematics show the shape of the potential with respect to twist angle, with the phase particle in the same well before switching. (**G**) Difference between positive and negative $\Delta J_{\text{c}} = \left|J_{\text{C}+}^{\text{F}/\text{H}} - J_{\text{C}-}^{\text{F}/\text{H}}\right|$, normalized by average $J_{\text{avg}} = \left(J_{\text{C}+}^{\text{F}/\text{H}} + J_{\text{C}-}^{\text{F}/\text{H}}\right)/2$ measured at 30 K. Schematic shows corresponding potential shape near 45°, where the phase particle is in different wells before switching.

respectively. A subsequent test sweep measures a critical current whenever the RCSJ washboard potential is tilted sufficiently to overcome the potential barrier, giving rise to asymmetric critical current densities $|J_{C_{-}}^{\rm F}|$ and $|J_{C_{-}}^{\rm H}|$. Note that we can flip the polarity of this Josephson diode by flipping polarity of the training current (Fig. 4C). In this way, we repeatedly and controllably prepare the JJ into either ground state (Fig. 4D). At higher temperatures, the phase dynamics become damped, which hinders the processes depicted in Fig. 4A by trapping ϕ in the local minima of the washboard potential. As a result, the $J_{\rm C}^{\rm F/H}$ asymmetry becomes less prominent upon heating and vanishes at about 50 K (Fig. 4E).

In this study, we investigated the Josephson diode effect in several JJs with different twist angles. For each JJ, the critical current difference $\Delta J = J_{\text{C}\pm}^{F/H} - J_{\text{C}\mp}^{H/F}$ reflects the asymmetry in potential barriers for each $\pm \phi_0$ valley (Fig. 4F), whereas the difference $\Delta J_{\text{c}} = J_{\text{C}+}^{F/H} - J_{\text{C}-}^{F/H}$ reflects asymmetries between the two free energy minima (Fig. 4G). In both cases, the differences are strongest near 43° and weaken at both 45° and ~35°, where j_1 and j_2 terms become negligible, respectively. Away from 45°, the absence of the diode effect is caused by the restoration of time-reversal symmetry. At exactly 45°, on the other hand, the purely secondharmonic Josephson potential has an additional symmetry around $\pm \varphi_0$: $\pm \varphi_0 \pm \varphi \leftrightarrow \pm \varphi_0 \mp \varphi$, which forbids the diode effect. Therefore, the diode effect is expected to vanish at 45° and at sufficiently low twist angles, which is consistent with our results. Thus, the observed diode effect is closely related to the free energy landscape of coexisting first- and second-harmonic CPR terms. The asymmetry between the two ground state valleys as observed in Fig. 4G can arise from an additional $\cos \varphi$ term in the CPR [see section S14 of (34) for details]. Our demonstration of the polarity-tunable Josephson diode effect in near-45° twist BSCCO JJs thus provides strong experimental evidence for TRS broken superconductivity based on the emergent interfacial SOP.

REFERENCES AND NOTES

- R. Ribeiro-Palau et al., Science 361, 690–693 (2018).
- 2. H. Yoo et al., Nat. Mater. 18, 448-453 (2019).
- S. Carr, S. Fang, E. Kaxiras, Nat. Rev. Mater. 5, 748–763 (2020).
- 4. D. M. Kennes et al., Nat. Phys. 17, 155–163 (2021).
- 5. Y. Cao et al., Nature 556, 43-50 (2018).
- 6. X. Lu et al., Nature 574, 653-657 (2019).
- '. Y. Saito et al., Nat. Phys. **17**, 478–481 (2021).
- 8. Y. Zhou et al., Nature 595, 48-52 (2021).
- 9. Y. Cao et al., Nature 556, 80-84 (2018).

- 10. M. Sigrist, Prog. Theor. Phys. 99, 899-929 (1998).
- Z. Yang, S. Qin, Q. Zhang, C. Fang, J. Hu, *Phys. Rev. B* 98, 104515 (2018)
- 12. O. Can et al., Nat. Phys. 17, 519-524 (2021).
- P. Volkov, J. Wilson, K. Lucht, J. Pixley, *Phys. Rev. B* 107, 174506 (2023).
- P. A. Volkov, J. H. Wilson, K. P. Lucht, J. H. Pixley, *Phys. Rev. Lett.* 130, 186001 (2023).
- 15. R. A. Klemm, Philos. Mag. 85, 801-853 (2005).
- 16. K. Schlenga et al., Phys. Rev. B 57, 14518-14536 (1998).
- 17. S. Y. F. Zhao et al., Phys. Rev. Lett. 122, 247001 (2019).
- 18. M. Liao et al., Nano Lett. **18**, 5660–5665 (2018). 19. Y. Yu et al., Nature **575**, 156–163 (2019).
- H. Hilgenkamp, J. Mannhart, Rev. Mod. Phys. 74, 485–549 (2002).
- C. C. Tsuei, J. R. Kirtley, Rev. Mod. Phys. 72, 969–1016 (2000).
- 22. F. Lombardi et al., Phys. Rev. Lett. **89**, 207001 (2002).
- 23. E. Il'ichev et al., Phys. Rev. Lett. 81, 894-897 (1998).
- E. Goldobin, D. Koelle, R. Kleiner, A. Buzdin, *Phys. Rev. B* 76, 224523 (2007).
- 25. L. J. Sandilands et al., Phys. Rev. B 90, 081402 (2014).
- 26. M. Fratini et al., Nature 466, 841-844 (2010).
- 27. Q. Li et al., Phys. Rev. Lett. 83, 4160-4163 (1999)
- Y. I. Latyshev, A. P. Orlov, A. M. Nikitina, P. Monceau, R. A. Klemm, *Phys. Rev. B* 70, 094517 (2004).
- 29. Y. Zhu et al., Phys. Rev. X 11, 031011 (2021).
- 30. Y. Takano et al., Phys. Rev. B 65, 140513 (2002).
- 31. J. Lee et al., Nano Lett. 21, 10469-10477 (2021).
- 32. Y. Zhu et al., Phys. Rev. B 57, 8601-8608 (1998).
- 33. Y. Takano et al., Physica C 408-410, 296-299 (2004).
- See supplementary materials for methods and detailed analysis.
- 35. N. Poccia et al., Phys. Rev. Mater. 4, 114007 (2020).
- N. B. Othman, G.-i. Oya, M. Kitamura, A. Irie, *IEEE Trans. Appl. Supercond.* 21, 176–179 (2011).
- 37. K. Hirata, S. Ooi, T. Mochiku, *Physica C* **362**, 114–120 (2001)
- G. Hechtfischer et al., Phys. Rev. B 55, 14638–14644 (1997).
- A. Yurgens, Supercond. Sci. Technol. 13, R85–R100 (2000).
- K. Tanabe, Y. Hidaka, S. Karimoto, M. Suzuki, *Phys. Rev. B* 53, 9348–9352 (1996).
- 41. A. Irie et al., Phys. Rev. B 62, 6681–6686 (2000).
- A. Barone, G. Paterno, Physics and Applications of the Josephson Effect (Wiley, 1982).
- M. Hashimoto, I. M. Vishik, R.-H. He, T. P. Devereaux, Z.-X. Shen, *Nat. Phys.* 10, 483–495 (2014).
- T. Tummuru, S. Plugge, M. Franz, *Phys. Rev. B* **105**, 064501 (2022).
- 45. H. Sickinger et al., Phys. Rev. Lett. 109, 107002 (2012).
- 46. A. Zyuzin, B. Spivak, *Phys. Rev. B* **61**, 5902–5904 (2000).
- 47. A. Buzdin, A. Koshelev, *Phys. Rev. B* **67**, 220504 (2003).
- N. G. Pugach, E. Goldobin, R. Kleiner, D. Koelle, *Phys. Rev. B* 81, 104513 (2010).
- 49. S. Scharinger et al., Phys. Rev. B 81, 174535 (2010).
- W. K. Neils, D. J. Van Harlingen, Phys. Rev. Lett. 88, 047001 (2002).
- 51. J. Mannhart et al., Phys. Rev. Lett. 77, 2782-2785 (1996).
- H. Hilgenkamp, J. Mannhart, B. Mayer, *Phys. Rev. B* 53, 14586–14593 (1996).
- A. C. Yuan, Y. Vituri, E. Berg, B. Spivak, S. A. Kivelson, *Phys. Rev. B* **108**, L100505 (2023).
- M. Tinkham, Introduction to Superconductivity (Dover Publications Inc., 1996).
- 55. K. Misaki, N. Nagaosa, Phys. Rev. B 103, 245302 (2021).
- 56. H. Wu et al., Nature **604**, 653–656 (2022).
- 57. M. Davydova, S. Prembabu, L. Fu, *Sci. Adv.* **8**, eabo0309 (2022)
- 58. J. Díez-Mérida et al., Nat. Commun. 14, 2396 (2023).
- C. Baumgartner et al., Nat. Nanotechnol. 17, 39–44 (2022).

- J. F. Steiner, L. Melischek, M. Trahms, K. J. Franke, F. von Oppen, Phys. Rev. Lett. 130, 177002 (2023).
- Y. Zhang, Y. Gu, P. Li, J. Hu, K. Jiang, Phys. Rev. X 12, 041013 (2022).
- 62. C. Baumgartner et al., J. Phys. Condens. Matter **34**, 154005 (2022).
- R. S. Souto, M. Leijnse, C. Schrade, *Phys. Rev. Lett.* 129, 267702 (2022).
- 64. B. Pal et al., Nat. Phys. **18**, 1228–1233 (2022).
- X. Cui et al., Replication Data for: Time-Reversal Symmetry Breaking Superconductivity between Twisted Cuprate Superconductors, version 1, Harvard Dataverse (2023); https://doi.org/10.7910/DVN/BYQDSP.

ACKNOWLEDGMENTS

The authors are grateful for sample shipping coordination with J. Y. Park and for fruitful discussions with D. K. Bediako, K. S. Burch,

S. Chakram, G.-H. Lee, R. Mélin, J. Wilson, B. Spivak, and S. Kivelson, Funding: The experiments were supported by the NSF (DMR-1809188 and DMR-1922172). P.K. acknowledges support from the US Department of Defense (DOD) Vannevar Bush Faculty Fellowship NO0014-18-1-2877 Work at the University of British Columbia was supported by NSERC and CFREF. Stencil masks were fabricated at Harvard CNS, a part of the National Nanotechnology Coordinated Infrastructure (NSF 1541959). STEM imaging was performed at Harvard CNS Imaging and Analysis Facility (NSF ECCS-2025158) and at Seoul National University. N.P. acknowledges the Deutsche Forschungsgemeinschaft (DFG-452128813) for partial support of the project. P.A.V. is supported by a Rutgers Center for Materials Theory Postdoctoral Fellowship, and J.H.P. is partially supported by the Air Force Office of Scientific Research under grant FA9550-20-1-0136, NSF CAREER grant DMR-1941569, and the Alfred P. Sloan Foundation through a Sloan Research Fellowship. P.A.V. and J.H.P. acknowledge the Aspen Center for Physics, where part of this work was performed, which is supported by National Science Foundation grant PHY-1607611. This work was partially supported by a grant from the Simons Foundation (P.A.V.). The work at Brookhaven National Laboratory was supported by the US Department of Energy, Office of Basic Energy Sciences, under contract DOE-sc0012704. Author contributions: S.Y.F.Z., N.P., and P.K. conceived of and designed the experiment. S.Y.F.Z. and N.P. developed the air-sensitive cryogenic stacking technique. S.Y.F.Z., X.C., and N.P. performed the experiments. S.L., M.K., H.Y., A.J.A., J.A.G., and R.E. performed the focused ion beam lamella sample preparation and TEM and STEM imaging, R.Z. and G.G. provided the crystals, P.A.V. and J.H.P. performed theoretical analysis of the Fraunhofer patterns and contributed to the analysis of the critical current. M.F., S.P., and T.T. performed theoretical analysis of the critical current. S.Y.F.Z., N.P., X.C., and P.K. analyzed the data and wrote the manuscript, with contributions from P.A.V., J.H.P., M.F., and Y.R Competing interests: The authors declare that they have no competing interests. Data and materials availability: The data from this study are available at the Harvard Dataverse (65). License information: Copyright © 2023 the authors, some rights reserved; exclusive licensee American Association for the Advancement of Science. No claim to original US government

SUPPLEMENTARY MATERIALS

science.org/doi/10.1126/science.abl8371 Materials and Methods Supplementary Text Figs. SI to S24 Table S1

Table S1 References (66–99)

article-reuse

Submitted 8 August 2021; resubmitted 7 February 2023 Accepted 7 November 2023

works. https://www.science.org/about/science-licenses-journal-

Published online 7 December 2023 10.1126/science.abl8371